International Journal of Engineering Science 226 (2026) 104563

Contents lists available at ScienceDirect

International Journal of Engineering Science

journal homepage: www.elsevier.com/locate/ijengsci

Full length article

Large deformations generated by the purely angular shear

Federico Oyedeji Falope, Luca Lanzoni *, Angelo Marcello Tarantino

DIEF, Università di Modena e Reggio Emilia, via P. Vivarelli 10, 41125, Modena, Italy

ARTICLE INFO

Keywords:
Finite elasticity
Hyperelasticity
Shear deformation
Pure shear
Simple shear
Purely angular shear
Compressible materials

ABSTRACT

In order to overcome some formal ambiguities and the difficulties encountered in the application of classical shear models in experimental tests, the authors have recently proposed a new methodology to the problem that naturally extends the pure shear paradigm of linearized elasticity to the finite elasticity. In this paper, the governing equations of the purely angular shear are transformed so that they can be applied directly in experimental investigations, and numerical and experimental analyses are then developed. In particular, for this last analysis, a specific testing machine, which foresees the monitoring of the test by a Digital Image Correlation (DIC) instrumentation, was designed and built. The results provided by the three different approaches are compared with each other, with the ultimate goal of making the shear behavior of a material that can experience large deformations more comprehensible.

1. Introduction

In linearized elasticity, the simple and pure shear models differ by an infinitesimal rigid rotation. When these two classical shear approaches are formulated in the context of finite elasticity, their response changes radically. In fact, considering two orthogonal material fibers, these are not only rotated but also elongated, to a different extent depending on the shear modes. Consequently, in finite elasticity, these two shear models must be considered truly physically different, producing dissimilar displacement, deformation, and stress fields.

Inspired by the linearized elasticity, Rivlin (1948) (Rivlin, 1948) was the first to adopt the form of the classic linear displacement field to describe the simple shear also in the framework of finite elasticity. This way of approaching the problem has been studied for a long time and is illustrated by many scientific texts, for example, Truesdell and Noll (Truesdell & Noll, 1965), Green and Zerna (Green & Zerna, 1968), Ogden (Ogden, 1984) and Gurtin, Fried and Anand (Gurtin et al., 2010). The simple shear, however, deserves credit for having highlighted some key features for the nonlinear theory, first of all the presence of normal stresses in addition to shear stresses. In particular, to maintain a simple shear plane deformation, it is necessary to apply to the sample the corresponding two in-plane shear stress components, but also normal stress components.[1] It is evident that these implications on the stress state greatly complicate the experimental analyses and require an accurate evaluation of the normal stress components.

Pure shear is achieved by subjecting a sheet to uniaxial extension.[2] The deformation is measured with respect to a reference system rotated by $\pi/4$ with respect to the direction of extension. Moreover, the deformation takes the form of a pure shear only in the central part of the sheet since the lateral edges tend to curve and this effect propagates inwards to a certain extent (Ogden, 1984), Rivlin and Saunders (1951) and Treloar (1975). The first pure shear experiments on thin sheets of rubber-like material were

* Corresponding author.
E-mail addresses: federicooyedeji.falope@unimore.it (F.O. Falope), luca.lanzoni@unimore.it (L. Lanzoni), angelomarcello.tarantino@unimore.it (A.M. Tarantino).

[1] In finite elasticity, a plane state of shear deformation is not associated with a plane state of stress, as is always the case in linearized elasticity.

[2] The term "pure" has been used as a synonym for irrotational.

https://doi.org/10.1016/j.ijengsci.2026.104563
Received 15 February 2026; Received in revised form 27 March 2026; Accepted 27 April 2026
Available online 17 May 2026

performed by Treloar (1944) (Treloar, 1944). In the pure shear, the in-plane dimension orthogonal to the extension direction is preserved (while the thickness of the sheet deforms freely). Namely, an in-plane principal stretch is kept unitary. This internal constraint is not easy to reproduce in practice.

There are many contributions in the literature for simple and pure shear. One of the most interesting aspects recently debated concerns the demonstration that a (plane) pure shear stress state produces a deformation field that does not coincide with the simple shear deformation, but with a simple shear deformation superimposed upon a triaxial stretch (see Moon and Truesdell (Moon & Truesdell, 1974), Mihai and Goriely (Mihai & Goriely, 2013), Destrade, Murphy and Saccomandi (Destrade et al., 2012) and Thiel et al. (2019)).

Horgan and Murphy (Horgan & Murphy, 2010) showed that some ambiguities in the formulation of simple shear arising in the determination of the arbitrary hydrostatic pressure term for the case of incompressible materials. These difficulties can be overcome by adopting a slight volumetric compressibility similar to that usually assumed in the finite element simulation of rubbers. The same authors (Horgan & Murphy, 2022) have demonstrated that, for generalized neo-Hookean materials, the corresponding deformation is that of plane strain with no out-of-plane stretch. The situation becomes more complicated when even the second invariant of the Cauchy–Green deformation tensor is included in the constitutive law. For example, in the case of a Mooney–Rivlin material, it was shown that a contractile out-of-plane stretch is required and that there is a coupled relationship between plane and out-of-plane stretches.

Moreira and Nunes (Moreira & Nunes, 2013) were the first to state that in the case of plane shear and compressible materials there is no correlation between a simple shear and a pure shear, namely a simple shear cannot be considered as pure shear combined with a rotation when large deformation is assumed.

Both simple and pure shear generate (unlike the corresponding linearized elasticity strain shear modes) kinematic effects due to both angular and extension deformations. This coupling can create uncertainties in the constitutive modeling and generates difficulties in investigating the shear behavior of a material. These considerations motivated the authors to propose the purely angular shear (Falope et al., 2026). In practice, the pure shear of the linearized elasticity has been generalized by supposing that the shear strains can become large. Thus, the purely angular shear is based only on the angular variation of linear elements and not on their extension.

Fig. 1 illustrates the three different shear deformations. The main peculiarities, in terms of deformation tensors and associated stress response for each of them, are synthesized below.

The deformation of simple shear is (cf. Fig. 1(b)[3,4]

$$\begin{cases} x = X + kY \\ y = Y \\ z = Z \end{cases}, \tag{1}$$

where k is a large positive constant called the amount of shear. The length of the material fibers along the Y and Z axes are held constant. This deformation preserves area and volume. From (1), the following Green–St.Venant $\mathbf{E}$ and Cauchy stress $\mathbf{T}$ tensors[5] can be computed (Falope et al., 2026):

$$[\mathbf{E}] = \frac{1}{2}\begin{bmatrix} 0 & k & 0 \\ k & k^2 & 0 \\ 0 & 0 & 0 \end{bmatrix}, \qquad [\mathbf{T}] = \begin{bmatrix} \mathrm{T}_{xx} & \mathrm{T}_{xy} & 0 \\ \mathrm{T}_{xy} & \mathrm{T}_{yy} & 0 \\ 0 & 0 & 0 \end{bmatrix}. \tag{2}$$

In the Green–St.Venant tensor, $\mathbf{E} = \frac{1}{2}\left(\mathbf{H} + \mathbf{H}^{\mathrm{T}} + \mathbf{H}^{\mathrm{T}}\mathbf{H}\right)$, where $\mathbf{H}$ is the displacement gradient, the quadratic component $\mathrm{E}_{yy} = \frac{1}{2}\left(\frac{\partial u}{\partial Y}\right)^2 = \frac{1}{2}k^2$ is due to an extensional deformation. In fact, the material fibers, originally oriented along the Y axis, are inclined and elongated (cf. Fig. 1(b). Thus, simple shear deformation produces combined angular and extensional deformation effects. The Cauchy stress tensor shows how the simple shear generates, in addition to the two tangential components, also different normal stress components.

The deformation of pure shear is (cf. Fig. 1(c)

$$\begin{cases} x = X + \frac{1}{2}(X+Y)\left(\lambda_2 - 1\right) \\ y = Y + \frac{1}{2}(X+Y)\left(\lambda_2 - 1\right) \\ z = \lambda_3 Z \end{cases}, \tag{3}$$

where the principal stretch λ_1 is set equal to one, λ_2 is the other in-plane principal stretch and λ_3 is the out-of-plane principal stretch. From (3), the following Green–St.Venant $\mathbf{E}$ and Cauchy stress $\mathbf{T}$ tensors can be computed (for more details, see eqns (28)-(32)

[3] The variables (X, Y, Z) indicate the coordinates of a generic material point P in the undeformed configuration, while the triple (x, y, z) corresponds to the position of the same point in the deformed configuration.

[4] Obviously, similar definitions apply to the XZ and YZ planes.

[5] In the three shear models, the condition $\mathrm{T}_{zz} = 0$ is imposed to calculate the out-of-plane principal stretch in the case of compressible materials and the reactive pressure in the case of incompressible materials.

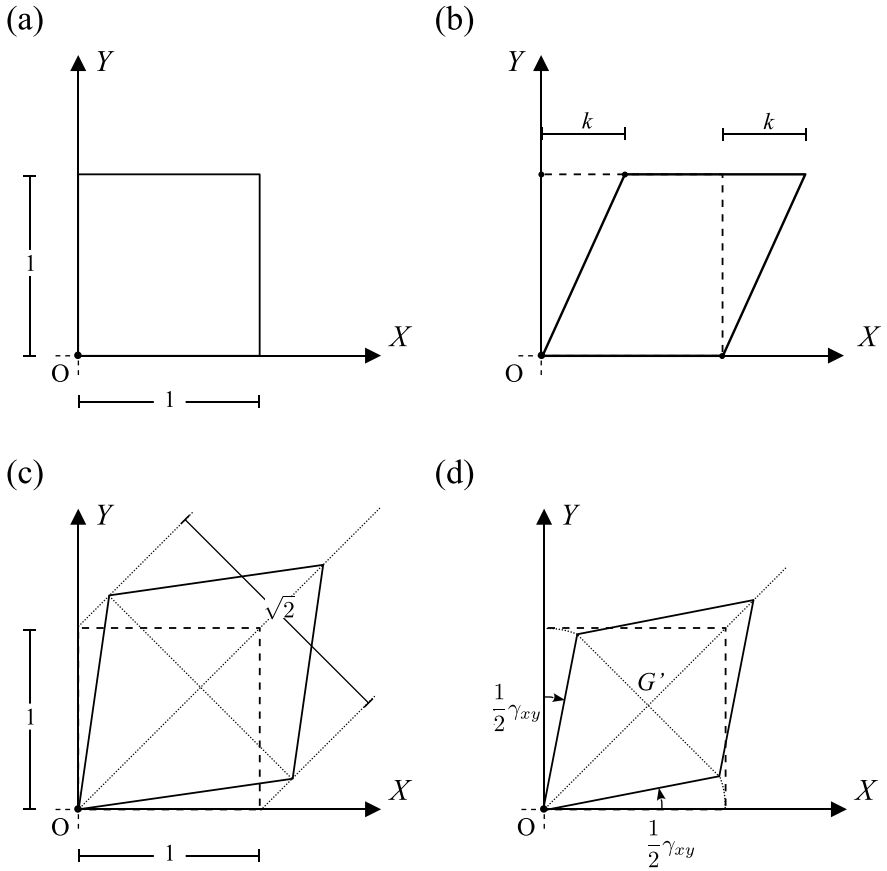

Fig. 1. Shear deformation modes in finite elasticity. Two-dimensional representation. Undeformed configuration (a). Simple shear (b). Pure shear. Case with $\lambda_2 > \lambda_1 = 1$. Principal direction 2 is parallel to the bisector (c). Purely angular shear (d).

of Falope et al. (2026)):

$$[\mathbf{E}] = \frac{1}{2}\begin{bmatrix} \frac{1}{2}\left(\lambda_2^2-1\right) & \frac{1}{2}\left(\lambda_2^2-1\right) & 0 \\ \frac{1}{2}\left(\lambda_2^2-1\right) & \frac{1}{2}\left(\lambda_2^2-1\right) & 0 \\ 0 & 0 & \lambda_3^2-1 \end{bmatrix}, \qquad [\mathbf{T}] = \begin{bmatrix} \mathrm{T}_{xx} & \mathrm{T}_{xy} & 0 \\ \mathrm{T}_{xy} & \mathrm{T}_{xx} & 0 \\ 0 & 0 & 0 \end{bmatrix}. \tag{4}$$

The Green–St.Venant tensor contains the two shear deformation components, $\mathrm{E}_{xy} = \mathrm{E}_{yx}$, but also two in-plane components, $\mathrm{E}_{xx} = \mathrm{E}_{yy}$, due to extensional deformations. In fact, the two material fibers, originally oriented along the X axis and Y axis (cf. Fig. 1(c), are rotated and elongated. Therefore, also the pure shear deformation (as well as the simple shear deformation) produces combined angular and extensional deformation effects. As in the previous case of simple shear, also for the pure shear, normal stress components are present in the Cauchy stress tensor. Now, $\mathrm{T}_{xx} = \mathrm{T}_{yy}$.

The deformation of purely angular shear is (cf. Fig. 1d) (Falope et al., 2026)

$$\begin{cases} x = \frac{1}{2}\left(\lambda_1+\lambda_2\right)X + \frac{1}{2}\left(\lambda_1-\lambda_2\right)Y \\ y = \frac{1}{2}\left(\lambda_1-\lambda_2\right)X + \frac{1}{2}\left(\lambda_1+\lambda_2\right)Y \\ z = \lambda_3 Z \end{cases}. \tag{5}$$

From (5), the following Green–St.Venant **E** and Cauchy stress **T** tensors can be computed:

$$[\mathbf{E}] = \begin{bmatrix} 0 & \frac{1}{4}\left(\lambda_1^2-\lambda_2^2\right) & 0 \\ \frac{1}{4}\left(\lambda_1^2-\lambda_2^2\right) & 0 & 0 \\ 0 & 0 & \frac{1}{2}\left(\lambda_3^2-1\right) \end{bmatrix}, \qquad [\mathbf{T}] = \begin{bmatrix} \mathrm{T}_{xx} & \mathrm{T}_{xy} & 0 \\ \mathrm{T}_{xy} & \mathrm{T}_{xx} & 0 \\ 0 & 0 & 0 \end{bmatrix}. \tag{6}$$

Unlike the two previous shear models, the normal components E_{xx} and E_{yy} are now zero. Usually, in-plane deformation generates out-of-plane deformation. Thus, inevitably, the E_{zz} component also appears in **E**. To produce a purely angular shear deformation

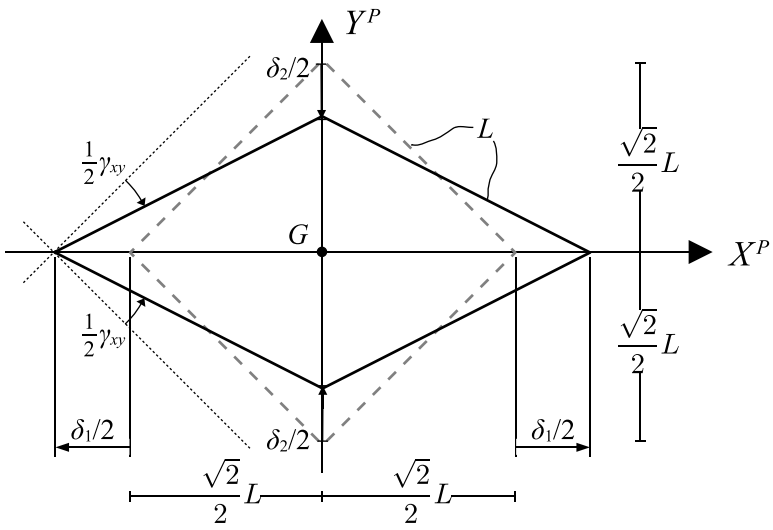

Fig. 2. Displacements in the XY plane generated by the purely angular shear model. Geometric details.

it is necessary to apply an in-plane equibiaxial normal stress $T_{xx} = T_{yy}$, in addition to the tangential stress T_{xy}. Therefore, unlike linearized elasticity, these in-plane normal stress components are associated with null in-plane normal deformation components.

This paper is devoted to the measure of large purely angular shear deformation to investigate the shear behavior of a material. With this purpose, theoretical, numerical and experimental analyses will be developed. The paper is organized as follows. The biaxial purely angular shear model is illustrated in Section 2. With respect to the principal reference system, the displacement, deformation, and stress fields, useful for experimental analyses, are derived. In Section 3, numerical analyses are performed using the finite element method. Section 4 concerns the experimental analysis. In particular, specific test equipment was designed and built for it. The results obtained with the three different approaches are compared with each other. Section 5 closes the paper summarizing the obtained results.

2. Governing equations

Let us consider a hyperelastic body $\mathcal{B}$ composed of a homogeneous, isotropic and compressible material.[6] Since only homogeneous deformations are considered, the shape of body is irrelevant, however, for sake of convenience, we assign the shape of a cube to the body $\mathcal{B}$. The symbol L will be used to indicate the length of the side of such a cube.

To derive the typical displacement field of some well-known experimental shear tests, such as the diagonal compression test or the picture frame test, it is useful to represent the displacements with respect to a principal reference system. Therefore, we will not use the generic reference system used in Fig. 1d, but the principal one $\{G, X^p, Y^p, Z^p\}$, with $(X^p, Y^p) : |X^p| + |Y^p| \leq L/\sqrt{2}$, and $0 < Z^p < L$. To illustrate the deformation produced by the purely angular shear model, we refer to the cross section of the cube belonging to the XY plane. This cross section (and all the sections parallel to it) is transformed into a rhombus (whose four sides are equal) by changing only the angle γ_{xy} of large magnitude. The principal axes X^p and Y^p are oriented according to the diagonals of the cross section. The geometric details are shown in Fig. 2.

Assuming γ_{xy} to be positive and using the principal stretches, the displacements δ_1, δ_2 and δ_3 along the principal direction can be expressed as (see Fig. 2)

$$\delta_1 = L\sqrt{2}\left(\lambda_1 - 1\right), \quad \delta_2 = L\sqrt{2}\left(1 - \lambda_2\right) \quad \text{and} \quad \delta_3 = L\left(\lambda_3 - 1\right). \tag{7}$$

The representation of the displacement field in the principal system is the simplest, since the displacement components are decoupled, in the sense that the displacement component u depends only on the variable X, etc. Furthermore, since the deformation is homogeneous, the displacement components u, v, and w vary linearly. Therefore, given (7), the displacement field is

$$\begin{cases} u = \frac{X}{L\sqrt{2}}\delta_1 = -X^p + X^p\lambda_1 \\ v = -\frac{Y}{L\sqrt{2}}\delta_2 = -Y^p + Y^p\lambda_2 \\ w = \frac{Z}{L}\delta_3 = -Z^p + Z^p\lambda_3 \end{cases}. \tag{8}$$

[6] If the geometric dimensions of the body $\mathcal{B}$ are infinitesimal, the entire analysis carried out in this paper becomes " local", i.e., it is valid for a single material point even under conditions of non-homogeneous deformation.

From one of the right triangles of the rhombus in Fig. 2, the following relation can be easily obtained[7]:

$$\frac{1}{2}\left(\lambda_1^2+\lambda_2^2\right)=1. \tag{9}$$

For the purely angular shear problem, stretches λ_1 and λ_2 must always satisfy relation (9). In this respect, the shear problem examined differs from a generic biaxial stretching problem, where these two stretches can be arbitrary.

Applying the material gradient operator $\mathrm{Grad}(\cdot)$ to the displacement field (8) yields the displacement gradient $\mathbf{H}$. With the well-known relation: $\mathbf{F}=\mathbf{H}+\mathbf{I}$, where $\mathbf{I}$ denotes the identity tensor, the deformation gradient $\mathbf{F}$ is obtained[8]

$$\left[\mathbf{F}^p\right]=\begin{bmatrix}\lambda_1 & 0 & 0\\ 0 & \lambda_2 & 0\\ 0 & 0 & \lambda_3\end{bmatrix}. \tag{10}$$

Once the deformation gradient $\mathbf{F}$ is known, the Green–St.Venant tensor $\mathbf{E}=\frac{1}{2}\left(\mathbf{F}^{\mathrm{T}}\mathbf{F}-\mathbf{I}\right)$ can be determined

$$\left[\mathbf{E}^p\right]=\frac{1}{2}\begin{bmatrix}\left(\lambda_1^2-1\right) & 0 & 0\\ 0 & \left(\lambda_2^2-1\right) & 0\\ 0 & 0 & \left(\lambda_3^2-1\right)\end{bmatrix}, \tag{11}$$

where only the normal components appear, which are easy to measure experimentally. Note also that, given (9), $\mathrm{E}^p_{11}+\mathrm{E}^p_{22}=0$.

By imposing a rigid clockwise rotation of $\pi/4$ around the Z axis to Green–St.Venant tensor (11), the corresponding tensor $(6)_1$, evaluated in the reference system of Fig. 1d, is recovered (that is, $\mathbf{E}=\mathbf{Q}\mathbf{E}^p\mathbf{Q}^{\mathrm{T}}$)[9]

$$[\mathbf{E}]=\begin{bmatrix}\frac{\sqrt{2}}{2} & -\frac{\sqrt{2}}{2} & 0\\ \frac{\sqrt{2}}{2} & \frac{\sqrt{2}}{2} & 0\\ 0 & 0 & 1\end{bmatrix}\begin{bmatrix}\frac{1}{2}\left(\lambda_1^2-1\right) & 0 & 0\\ 0 & \frac{1}{2}\left(\lambda_2^2-1\right) & 0\\ 0 & 0 & \frac{1}{2}\left(\lambda_3^2-1\right)\end{bmatrix}\begin{bmatrix}\frac{\sqrt{2}}{2} & \frac{\sqrt{2}}{2} & 0\\ -\frac{\sqrt{2}}{2} & \frac{\sqrt{2}}{2} & 0\\ 0 & 0 & 1\end{bmatrix}= \tag{12}$$

$$\begin{bmatrix}0 & \frac{1}{4}\left(\lambda_1^2-\lambda_2^2\right) & 0\\ \frac{1}{4}\left(\lambda_1^2-\lambda_2^2\right) & 0 & 0\\ 0 & 0 & \frac{1}{2}\left(\lambda_3^2-1\right)\end{bmatrix}.$$

To obtain (12), relation (9) was used.

Using the expression (16) of Falope et al. (2026) and the above tensor $\mathbf{E}$, the expression of the shear deformation γ_{xy} is derived

$$\sin\gamma_{xy}=\frac{2\mathrm{E}_{xy}}{\sqrt{1+2\mathrm{E}_{xx}}\sqrt{1+2\mathrm{E}_{yy}}}=\frac{1}{2}\left(\lambda_1^2-\lambda_2^2\right). \tag{13}$$

After discussing the kinematic aspects, we now return to the principal reference system shown in Fig. 2 to evaluate the stress tensors. The constitutive properties of a hyperelastic material are described by the stored energy function ω. If the function ω is frame-indifferent, homogeneous and isotropic, then it depends only on the principal invariants I_i, with $i=1,2$ and 3, of the Cauchy–Green strain tensors. With these assumptions, the constitutive law ($\mathbf{T}_R=\partial\omega/\partial\mathbf{F}$) takes the following form:

$$\mathbf{T}_R=2\left(\frac{\partial\omega}{\partial I_1}+I_1\frac{\partial\omega}{\partial I_2}\right)\mathbf{F}-2\frac{\partial\omega}{\partial I_2}\mathbf{B}\mathbf{F}+2I_3\frac{\partial\omega}{\partial I_3}\mathbf{F}^{-\mathrm{T}}, \tag{14}$$

where the tensor $\mathbf{T}_R$ denotes the (first) Piola–Kirchhoff stress tensor. In the above expression, $\mathbf{B}=\mathbf{F}\mathbf{F}^{\mathrm{T}}$ is the left Cauchy–Green strain tensor. Piola–Kirchhoff stresses are the Lagrangian stresses, defined in the undeformed configuration, while the corresponding Eulerian stress measure is Cauchy stress, namely the stresses in the deformed configuration. The Cauchy stress tensor $\mathbf{T}$ can be obtained from the Piola–Kirchhoff stress tensor $\mathbf{T}_R$ through the following well-known transformation:

$$\mathbf{T}_R=\mathbf{T}\,\mathbf{F}^{\star}, \tag{15}$$

where $\mathbf{F}^{\star}=(\det\mathbf{F})\mathbf{F}^{-\mathrm{T}}$ is the cofactor of the tensor $\mathbf{F}$.[10] Using the displacement field (8), the tensors $\mathbf{F}^p$, $\mathbf{B}^p$, and $(\mathbf{F}^p)^{-\mathrm{T}}$ take the diagonal form, and formula (14) provides the principal Piola–Kirchhoff stress tensor

$$\left[\mathbf{T}^p_R\right]=\begin{bmatrix}\mathrm{T}^p_{R_{11}} & 0 & 0\\ 0 & \mathrm{T}^p_{R_{22}} & 0\\ 0 & 0 & \mathrm{T}^p_{R_{33}}\end{bmatrix}, \tag{16}$$

[7] In terms of displacements δ_1 and δ_2, formula (9) becomes:

$$\delta_1^2+2\sqrt{2}\,L\left(\delta_1-\delta_2\right)+\delta_2^2=0.$$

[8] The apex p indicates that the components of the tensor have been evaluated with respect to the principal reference system.

[9] The translation of the centroid G in the origin O has no effect on the performed calculation.

[10] The tensor $\mathbf{F}$ is invertible by its definition.

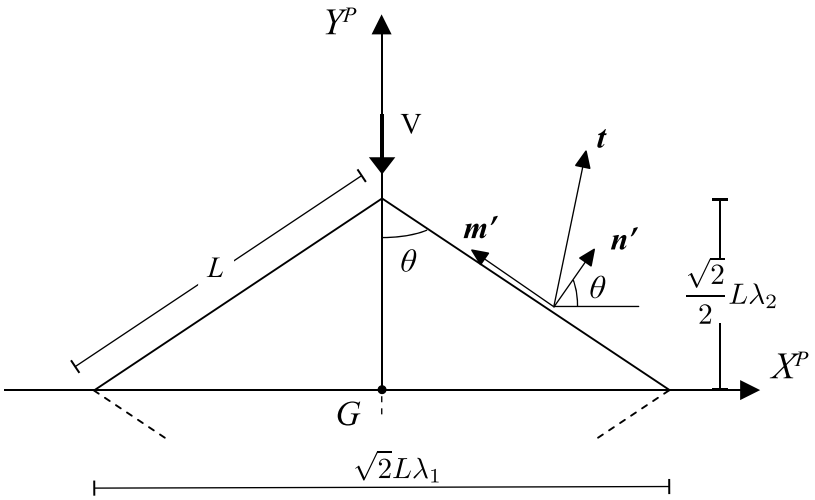

Fig. 3. Cauchy stress vector components of the inclined faces in the deformed configuration.

with

$$\mathrm{T}^p_{R_{11}} = 2\lambda_1\left[\omega_{,1} + 2\omega_{,2} + \lambda_3^2\omega_{,2} - \lambda_1^2\omega_{,2} + \lambda_2^2\lambda_3^2\,\omega_{,3}\right],$$

$$\mathrm{T}^p_{R_{22}} = 2\lambda_2\left[\omega_{,1} + 2\omega_{,2} + \lambda_3^2\omega_{,2} - \lambda_2^2\omega_{,2} + \lambda_1^2\lambda_3^2\,\omega_{,3}\right],$$

$$\mathrm{T}^p_{R_{33}} = 2\lambda_3\left[\omega_{,1} + 2\omega_{,2} + \lambda_1^2\lambda_2^2\,\omega_{,3}\right].$$

The boundary conditions, relating to the two faces of the cube with normals parallel to the Z axis, can be imposed by requiring that these two faces must be traction-free. Then, from condition $\mathrm{T}^p_{R_{33}} = 0$, an expression to calculate the principal stretch λ_3 is obtained

$$\omega_{,1} + 2\omega_{,2} + \lambda_1^2\lambda_2^2\,\omega_{,3} = 0. \tag{17}$$

With (17), the above principal Piola–Kirchhoff stress components can be rewritten as follows:

$$\begin{cases} \mathrm{T}^p_{R_{11}} = 2\lambda_1\left(\lambda_3^2 - \lambda_1^2\right)\left[\omega_{,2} + \lambda_2^2\,\omega_{,3}\right] \\ \mathrm{T}^p_{R_{22}} = 2\lambda_2\left(\lambda_3^2 - \lambda_2^2\right)\left[\omega_{,2} + \lambda_1^2\,\omega_{,3}\right] \\ \mathrm{T}^p_{R_{33}} = 0 \end{cases}. \tag{18}$$

By applying the transformation (15) to (18), the principal Cauchy stresses are obtained

$$\begin{cases} \mathrm{T}^p_{11} = \frac{2\lambda_1^2}{\lambda_1\lambda_2\lambda_3}\left(\lambda_3^2 - \lambda_1^2\right)\left[\omega_{,2} + \lambda_2^2\,\omega_{,3}\right] \\ \mathrm{T}^p_{22} = \frac{2\lambda_2^2}{\lambda_1\lambda_2\lambda_3}\left(\lambda_3^2 - \lambda_2^2\right)\left[\omega_{,2} + \lambda_1^2\,\omega_{,3}\right] \\ \mathrm{T}^p_{33} = 0 \end{cases}. \tag{19}$$

Using the Cauchy stress tensor $\mathbf{T}^p$, the distribution of stresses present in the inclined faces of the deformed cube can be evaluated. We refer to the upper face of the deformed cube, the trace of which is in the first quadrant of Fig. 3. Similar results are valid for the other three lateral faces. The unit vectors $\mathbf{n}'$ and $\mathbf{m}'$ of Fig. 3 have the following components: $\mathbf{n}' = (\cos\theta, \sin\theta, 0)$ and $\mathbf{m}' = (-\sin\theta, \cos\theta, 0)$, where $\sin\theta = \frac{\sqrt{2}}{2}\lambda_1$ and $\cos\theta = \frac{\sqrt{2}}{2}\lambda_2$, and they are orthogonal to each other, that is $\mathbf{n}' \cdot \mathbf{m}' = 0$.[11] The Cauchy stress vector $\mathbf{t}$ is directly evaluated by means of the following linearity relationship: $\mathbf{t}\left(P, \mathbf{n}'\right) = \mathbf{T}(P)\mathbf{n}'$. With respect to the inclined face, the normal and tangential components of the Cauchy stress vector are[12]

$$\mathrm{t}_{n'} = \mathbf{n}' \cdot \mathbf{T}^p\mathbf{n}' = \frac{\lambda_2^2}{2}\mathrm{T}^p_{11} + \frac{\lambda_1^2}{2}\mathrm{T}^p_{22}, \tag{20}$$

[11] The fundamental relation of trigonometry, $\sin^2\theta + \cos^2\theta = 1$, reproduces relation (9).

[12] By multiplying $\mathrm{t}_{n'}$ and $\mathrm{t}_{n'm'}$ by $\lambda_3 L^2$ it is immediate to obtain the normal force and the shear force acting on the inclined faces.

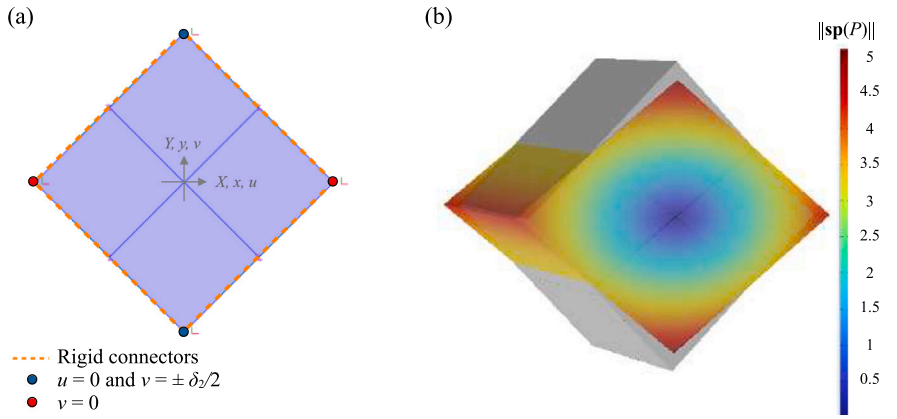

Fig. 4. FE model of the purely angular shear deformation. 2D plane stress model, rigid connectors, and boundary conditions (a). Contour plot of the displacement field norm in the deformed configuration (b).

$$\mathrm{t}_{n'm'} = \mathbf{m}' \cdot \mathbf{T}^p \mathbf{n}' = \frac{\lambda_1 \lambda_2}{2} \left(\mathrm{T}^p_{22} - \mathrm{T}^p_{11} \right). \tag{21}$$

These components are uniform along the inclined face.

In view of the experimental tests, Fig. 3 highlights the external vertical force V applied to deform the sample. The opposite corner is constrained and does not undergo displacements. Invoking equilibrium, and using (9), the force V is equal to

$$V = 2L^2 \lambda_3 \left(\mathrm{t}_{n'm'} \cos\theta + \mathrm{t}_{n'} \sin\theta \right) = \sqrt{2} L^2 \lambda_1 \lambda_3 \mathrm{T}^p_{22}, \tag{22}$$

where $\left(\sqrt{2} L \lambda_1\right) \left(L \lambda_3\right)$ is the cross-sectional area of the deformed cube in the $X^p Z^p$ plane. This force should be interpreted here as the vertical resultant necessary to balance the applied stresses. In practical applications, the cube will be confined by a rigid structure with hinges along the edges, and the force V will be reformulated (cf. (23)).

3. Numerical analysis

To formulate the boundary value problem, keep in mind that since the deformations are homogeneous, the stresses do not vary at internal points of the body. Therefore, if the body forces are assumed to be zero, the local equilibrium equations are automatically satisfied. The boundary value problem is therefore reduced to the sole imposition of boundary conditions. In particular, the stresses at the boundary (including zero stresses on the two faces with normals parallel to the Z^p axis) can be interpreted as the external surface forces necessary to produce the displacement field (8).

To perform a comparison between the exact analytical solution and the numerical solution, the sample, subjected to biaxial purely angular shear, is modeled by using the FE code COMSOL Multiphysics v.6.1. 2D plane elements under plane stress condition are used in the FE code, whose discretized model is displayed by Fig. 4. On each side, a system of rigid connectors is applied, which guarantees that the length of the sides themselves is maintained. The vertical component of the displacement field of the red nodes of Fig. 4a is prevented, while the horizontal component is restrained to the blue nodes. A nonlinear incremental analysis is carried out under displacement control. The kinematic control parameter of the analysis is the prescribed vertical displacement of the blue nodes. Upper and lower blue nodes are subjected to opposite prescribed displacements corresponding to $\delta_2/2$. The incremental step of such prescribed displacements is $L/100$.

Since the deformation is homogeneous, namely independent of the spatial variables, the use of serendipity quadratic shape functions makes the FE solution exact. Therefore, the problem is mesh independent. However, we have opted to discretize the square rubber with 100 (10 × 10) quadrilateral elements of aspect ratio 1. The norm of the displacement field is sketched in Fig. 4b over the deformed configuration of the body.

The comparison between the analytical and numerical solutions is carried out below by evaluating stretches and stresses. As previously mentioned, the solutions of the two different analysis methods are perfectly overlapped over the entire range of deformation (i.e. the relative error is zero). Ultimately, numerical analyses will only serve to check analytical solutions.

4. Experimental analysis

To prepare specimens, a two-component polymer was cast into 3D-printed molds to form cuboidal blocks with a square cross section. These blocks have a side length L of 60 mm and thickness t of 30 mm (cf. Fig. 5a). A white pigment was added during the casting process to enhance the contrast between the material surface and the speckle pattern, thereby facilitating optical monitoring by the Digital Image Correlation (DIC) system. The DIC setup consists of four synchronized cameras (cf. Fig. 5b), enabling accurate measurement of both in-plane and out-of-plane deformations.

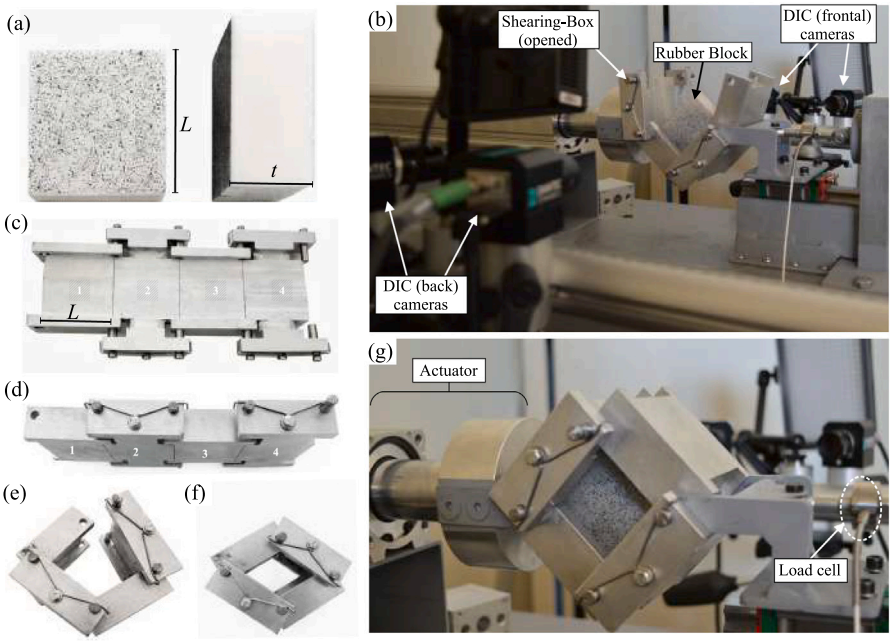

Fig. 5. Purely angular shear tests. Rubber specimens with square cross section of 60 × 60 mm^2 and thickness of 30 mm (a). Experimental device composed of a steel shearing-box with the rubber specimen, monitored with two pairs of DIC cameras placed on the frontal and back surface of the specimen for the in-plane and out-of-plane principal stretches monitoring (b). Details of the shearing box internal surface (c). Lateral view of the shearing box (d). Assembled final form of the empty shearing box opened (e) and closed (f). Test setup where the actuator drives the motion of the shearing box under purely angular shear deformation and load cell measures the applied force (g).

To carry out experimental tests, special equipment was designed and built. In detail, purely angular shear is simulated by placing the rubber block inside a steel shearing box (cf. Figs. 5c÷f). The shearing box consists of four thick steel plates connected by eight cylindrical hinges, highlighted in Figs. 5c and 5d. The shearing box containing the specimen is then mounted on the angular shear machine, where two opposite cylindrical hinges are connected to the actuator's anchoring system (left side of Fig. 5g) and to a load cell (right side of Fig. 5g) with a full-scale capacity of 1 kN ±0.1%. The actuator operates at a displacement rate of 50 mm/min in both directions.

Two virtual gauges are defined on the frontal surfaces of the rubber specimen using the DIC tools (cf. Fig. 6). The variation in gauge length is used to compute the in-plane principal stretches λ_1 and λ_2. Using DIC features, a point marker is defined at the intersection of the two gauges. Two cameras track the marker position on the front surface, while the other two cameras recognize and capture its projection on the back surface. The variation in distance between the original marker and its back-surface projection provides the through-the-thickness out-of-plane principal stretch λ_3.

Fig. 7 shows a succession of images taken during the test. In the first column the deformations of the rubber block are visible, while in the second column the lateral views of the acquired surfaces (frontal and back) with DIC at different values of the prescribed displacement δ_2 in the reference (green) and deformed configuration (red) are shown.

When the deformation becomes too severe, the sample tends to deform in an inhomogeneous way, as highlighted in the last image in Fig. 7. Some aspects related to sample collapse are discussed in Appendix A.

To deform the sample, two horizontal forces $\bar{V}$ must be applied in the hinges. In the testing machine built, one force $\bar{V}$ is generated by the actuator and the other is the constraint reaction of the opposite hinge which is fixed (cf. Fig. 5g). The steel plates that circumscribe the sample are much stiffer than the sample itself. During the test, stresses arise at the interface between the sample and the steel plates. The stresses exerted on the sample are the components of the Cauchy stress vector. The same stresses act in the rods but in opposite directions. The resultant forces of these stresses are (cf. Fig. 8): $F_x = L^2\lambda_3\, t_x = L^2\frac{\sqrt{2}}{2}\,\lambda_2\lambda_3\,\mathrm{T}^p_{11}$ and $F_y = L^2\lambda_3\, t_y = L^2\,\frac{\sqrt{2}}{2}\,\lambda_1\lambda_3\mathrm{T}^p_{22}$. The rotational equilibrium of the rod around the pole B shown in Fig. 8 gives: $-F_x\, L\frac{\sqrt{2}}{2}\,\lambda_2 - \frac{\bar{V}}{2}\,L\frac{\sqrt{2}}{2}\,\lambda_1 + F_y\, L\frac{\sqrt{2}}{4}\,\lambda_1 + F_x\, L\frac{\sqrt{2}}{4}\,\lambda_2 = 0$, from which an expression for the force $\bar{V}$ is obtained

$$\bar{V} = \frac{\sqrt{2}}{2}L^2\frac{\lambda_3}{\lambda_1}\left[\mathrm{T}^p_{22}\lambda_1^2 - \mathrm{T}^p_{11}\lambda_2^2\right]. \tag{23}$$

It is important to highlight the distinctive features of this new experimental setup as compared to classical shear testing configurations, as well as with respect to the concepts of energy exhaustiveness and full-field coverage characterization. Simple shear tests are typically performed by bonding a specimen between two parallel plates, which are then displaced, maintaining their

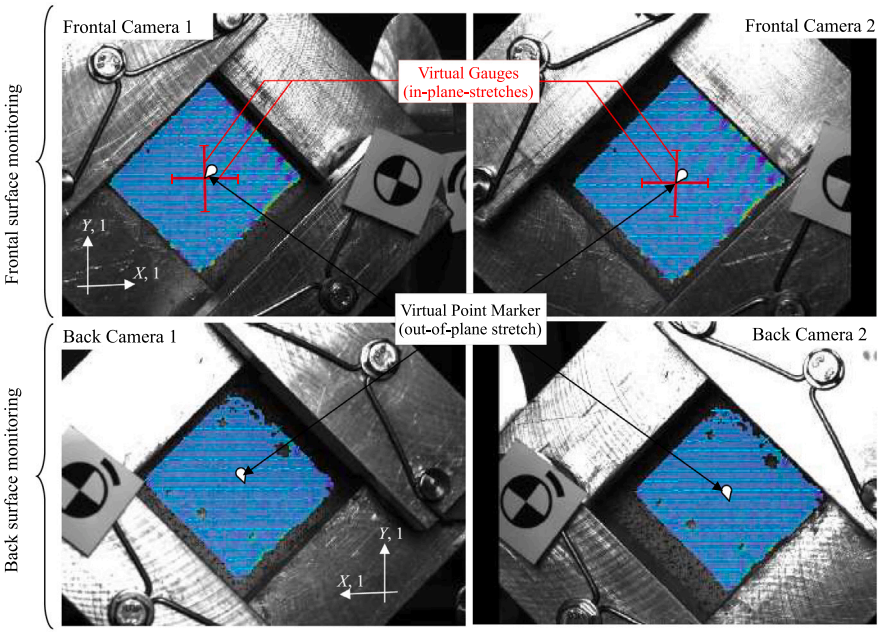

Fig. 6. Views of the four DIC cameras for the optical monitoring of the principal stretches: The blue dashed lines denote the principal direction 1, along with and orthogonal to it, the virtual gauges (red lines) are drawn to compute the in-plane principal stretches. At the intersection of the gauges, a marker (white point) is placed, recognized on both cameras (front and back surfaces), and it is used for the calculation of the principal out-of-plane stretch λ_3.

mutual orthogonal distance unchanged. However, such a setup does not properly reproduce the mechanical boundary conditions of an ideal simple shear state, in which the inclined surfaces are subjected to both normal and tangential tractions (e.g. Rivlin (1948) and Mihai and Goriely (2013)). This is not the case for the angular shear device proposed here. In the present experimental setup, all four lateral surfaces of the specimen are loaded, and the resulting prescribed deformation state is fully consistent with the theoretical formulation. With regard to the concepts of energy exhaustiveness (Falope et al., 2024) and full-field coverage characterization (Falope, 2026), the angular shear setup represents an energetically exhaustive test provided that the stress field at the interface between the specimen surfaces and the rigid plates is measured. Therefore, the proposed layout can be effectively used to improve the strength of a simultaneous identification procedure based on various experimental tests to properly characterize the strain energy function (Falope et al., 2024).

5. Results and comparisons

In Sections 2, the expression of the stored energy function ω was kept completely arbitrary. In the following, to be able to perform numerical applications, it is necessary to assign the form of ω. For this purpose, the compressible Mooney–Rivlin law is assumed[13,14]

$$\omega(I_1, I_2, I_3) = aI_1 + bI_2 + cI_3 - (a + 2b + c)\, lnI_3, \tag{24}$$

where the constants a, b and c are strictly positive quantities. It is well known that the above stored energy function, which depends on all three deformation invariants, describes properly the constitutive behavior of rubbers and rubber-like materials. From (24), the following derivatives can be computed:

$$\omega_{,1} = a, \quad \omega_{,2} = b, \quad \omega_{,3} = c - \frac{a + 2b + c}{I_3}, \tag{25}$$

[13] This function is polyconvex and satisfies the growth conditions: $\omega \to \infty$ as $\lambda \to 0^+$ or $\lambda \to +\infty$. It was used, for example, in Lanzoni and Tarantino (2018), Lanzoni and Tarantino (2020a), (Lanzoni & Tarantino, 2020b) and Falope et al. (2019).

[14] For an extensive discussion of the terms related to the volume change in the stored energy function see the recent paper by M. Pelliciari et al. (2023).

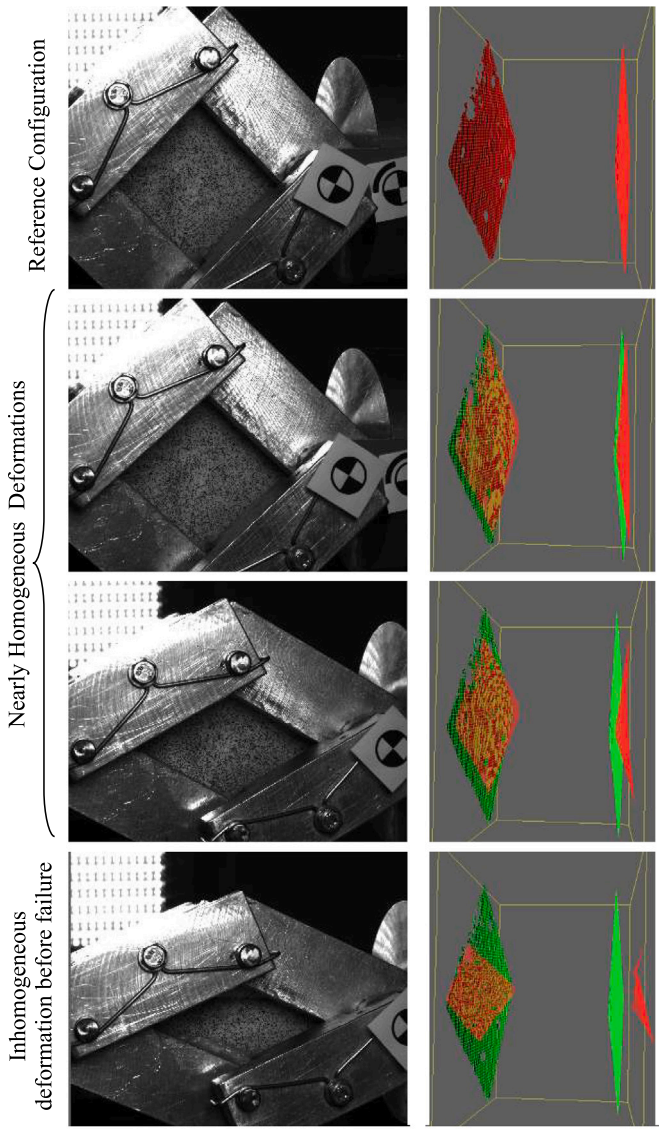

Fig. 7. Reference and deformed configurations acquired by the DIC cameras of the rubber block under prescribed displacement.

where $\omega_{,i} = \frac{\partial \omega}{\partial I_i}$, for $i = 1$, 2 and 3. With these three derivatives, the stress components (19) become

$$\begin{cases} \mathrm{T}^p_{11} = \frac{2\left(\lambda_1^2-\lambda_3^2\right)}{\lambda_1\lambda_2\lambda_3^3}\left[a + \left(2-\lambda_1^2\lambda_3^2\right)b + \left(1-\lambda_1^2\lambda_2^2\lambda_3^2\right)c\right] \\ \mathrm{T}^p_{22} = \frac{2\left(\lambda_2^2-\lambda_3^2\right)}{\lambda_1\lambda_2\lambda_3^3}\left[a + \left(2-\lambda_2^2\lambda_3^2\right)b + \left(1-\lambda_1^2\lambda_2^2\lambda_3^2\right)c\right] \\ \mathrm{T}^p_{33} = 0 \end{cases}, \tag{26}$$

while condition (17) provides

$$\lambda_3 = \sqrt{\frac{a+2b+c}{a+2b+\lambda_1^2\lambda_2^2 c}}. \tag{27}$$

Using (26), the normal and tangential components of the Cauchy stress vector acting on the deformed faces of the cube, (20) and (21), for a compressible Mooney–Rivlin material, can be readily evaluated. Note that, in the absence of deformation $\lambda_1 = \lambda_2 = \lambda_3 = 1$, all stresses vanish.

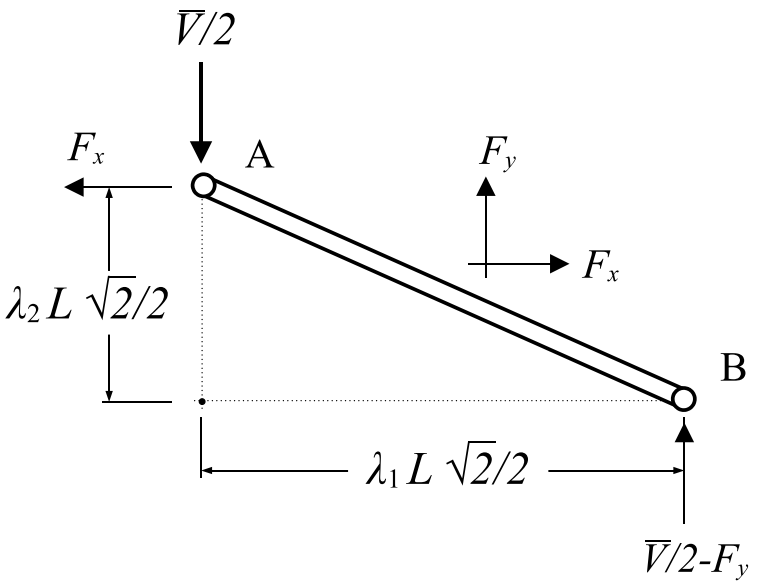

Fig. 8. Equilibrium of a rod forming the shearing box of the testing machine.

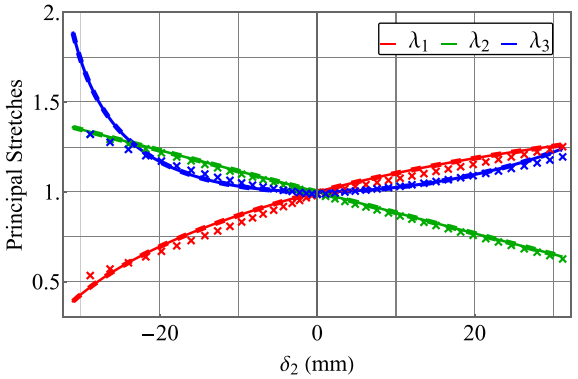

Fig. 9. Principal stretches λ_1, λ_2, and λ_3. Analytical (solid line) and numerical (dashed) results obtained for a Dragon Skin FX Pro silicone rubber, modeled as a compressible Mooney–Rivlin material, with the following constitutive parameters: $a = 19.43$, $b = 7.25$ and $c = 79.799$ kPa. The solid and dashed curves are perfectly overlapped. The experimental (cross-markers) results are measured with the DIC optical device.

In the following diagrams the results are shown as a function of the prescribed displacement δ_2. The analytical expressions of the principal stretches in terms of δ_2 are obtained by means of 7_2, (9) and (27). Subsequently, introducing these expressions into (26), the principal Cauchy stresses in terms of δ_2 are derived. With stretches and stresses in terms of δ_2, the force V, defined by (23), can also be determined as a function of δ_2, thus relating the applied external force and the vertical displacement produced at its point of application.

For the constitutive parameters present in the stored energy function (24), the following values are assumed: $a = 19.43$, $b = 7.25$ and $c = 79.799$ kPa, which have been estimated experimentally by the authors for specimens made of the silicone rubber Dragon Skin FX Pro and subjected to uniaxial tension and compression, torsion and unequal biaxial loading (Falope et al., 2024) and Falope et al. (2025).

Having defined the shape of the stored energy function, we now examine the results obtained with the three different approaches, illustrated in the previous Sections. In the figures that follow in this Section, the analytical results are shown with solid curves, the numerical ones with dashed lines, while the cross markers denote experimental quantities.

It is important to specify that in the experimental tests the kinematics undergone by the sample is available, the constitutive behavior is known (albeit in an approximate form) and the applied forces can be measured. So, everything is known, and the tests are performed with the aim of verifying the analyses carried out previously and comparing the results of the different approaches

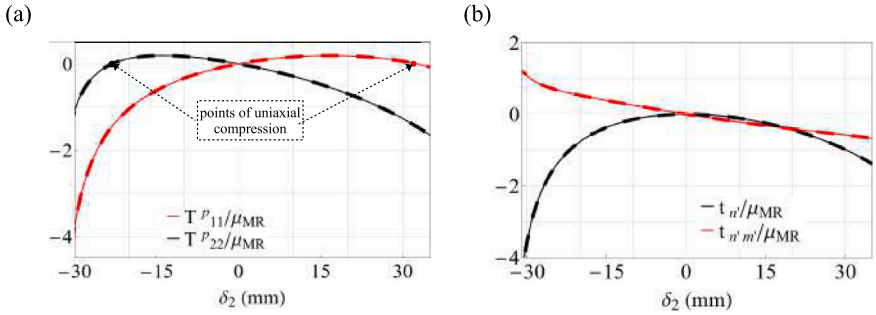

Fig. 10. Cauchy stresses. Components T^p_{11} and T^p_{22} (a). Cauchy stress vector components normalized with respect to the linearized shear modulus μ_{MR} (b).

with each other. Obviously, testing machines can be used for a different purpose, such as investigating the behavior of a material under shear deformation whose constitutive law is unknown.

The principal stretches λ_1, λ_2, and λ_3, obtained from three different approaches are shown in Fig. 9 as a function of the assigned displacement δ_2 along the Y^p axis. The stretch λ_1 (red line) occurs along the horizontal X^p axis of the principal reference system in Fig. 2. For positive δ_2 there is a horizontal extension of the block, while there is a contraction for negative δ_2. Note that the range of variation of δ_2, with respect to the side of the block, is quite large. Orthogonal to λ_1, the in-plane stretch λ_2 (green line) describes, along the Y^p axis, a monotonically increasing contraction for positive δ_2. When δ_2 is positive and grows further, the deviation (in absolute value) from the unit value is greater for λ_2 than for λ_1. This is because the stretch λ_2 governs a transformation that (ideally) reduces the initial segment of length $L\sqrt{2}$ to zero, while the stretch λ_1 describes the deformation that (ideally) transforms the initial segment still of length $L\sqrt{2}$ to the final segment of length $2L$. The situation is reversed for negative δ_2. For positive δ_2, the out-of-plane principal stretch λ_3 describes a monotonically increasing extension. This stretch starts with a unit value and horizontal slope and grows weakly in the initial part of the graph and then rises sharply, highlighting a strong transversal dilation of the block for large values of δ_2. The behavior is similar, but more pronounced, for negative δ_2, with λ_3 still greater than 1, essentially because during the test the cross-section decreases regardless of the sign of δ_2. Note that, regardless of the sign of δ_2, the specimen undergoes an out-of-plane expansion. In general, in the evaluation of principal stretches, a good agreement is observed between the analytical and experimental results, especially at lower levels of deformation. The increasing discrepancy in the out-of-plane principal stretches λ_3 is attributed to friction along the Z axis (see Appendix A).

In Fig. 10a, the principal Cauchy stresses T^p_{11} and T^p_{22} are plotted using (26). The numerical analysis provides coincident results. The experimental analysis carried out obviously does not provide local values of the stresses. For a positive δ_2, T^p_{22} is negative (compression) and T^p_{11} is positive (tension). The opposite occurs for a negative δ_2. Fig. 10b shows the normal and tangential components of the Cauchy stress vector (20) and (21), that is the stresses that arise on the inclined faces of the deformed sample. These stresses are normalized with respect to the linearized shear modulus of the Mooney–Rivlin material $\mu_{MR} = 2(a+b)$ [8]. The tangential component $t_{n'm'}$, which occurs in the same direction as γ_{xy} (or, similarly, that does positive work for γ_{xy}), initially has a linear trend (as happens in the linearized theory) and then (in absolute value) grows rapidly when δ_2 becomes large, denoting a strong nonlinear behavior. Given the normalization, the slope of the initial section of the curve is unity. For δ_2 positive, the normal component $t_{n'}$ is compressive, it starts from zero with zero slope (as happens in linearized elasticity) and grows rapidly with δ_2. Except in the initial part of the graph, the normal component $t_{n'}$ is, in absolute value, greater than the corresponding tangential component $t_{n'm'}$. These normal stresses become so strong that they can change the sign of the stress component T^p_{11} (cf. Fig. 10a). For δ_2 negative, similar considerations apply. In essence, unlike linearized elasticity, in finite elasticity to generate a shear angle γ_{xy} it is necessary to apply both shear and normal stresses in the XY plane.

Let us proceed with the comparison of other kinematic quantities. Based on the experimental results, relation (9) is plotted in Fig. 11a. To make the differences more evident, the ordinates of the graph are limited to a value around 2. This graph shows that, except for a few steps preceding specimen failure, the relative error remains limited to 2.5%. This result indirectly demonstrates the effectiveness of the test instrumentation designed and built for the purely angular shear. The normal component $t_{n'}$ is negative, implying that the volume decreases ($\sqrt{I_3} = \det \mathbf{F} = J \leq 1$). Fig. 11b shows the volume variation, confirming that, for moderate deformations, the silicone rubber behaves as nearly incompressible [14].

Finally, the force exerted by the actuator to deform the sample is considered. In Fig. 12, the normalized force $\bar{V}\sqrt{2}/Lt$ using (23) and the related experimental values are plotted (symbol t denotes the thickness of the sample). The results are in good agreement, however, a slight deviation, more pronounced under tension than under compression, can be observed for increasing δ_2. This discrepancy between the two curves can be attributed to a lower ability of the constitutive Mooney–Rivlin model to capture the tensile response of the silicone material [14].

The linearization of the purely angular shear model reproduces exactly the pure shear model of the linearized elasticity (Falope et al., 2026). For practical purposes, in the linear context, the diagonal compression test is the standard shear test. This test involves

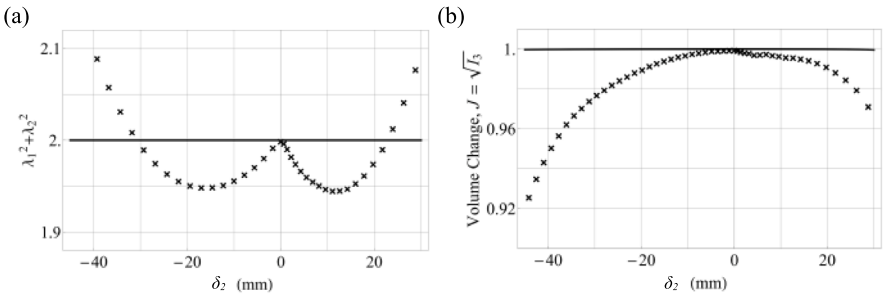

Fig. 11. Comparison of other kinematic quantities. Kinematic relation (9) (a). Volume variation (b).

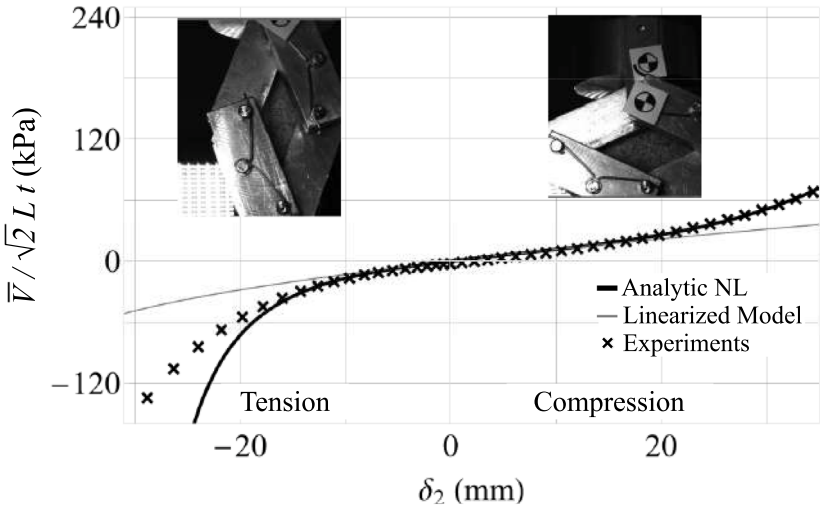

Fig. 12. Force $\bar{V}$ exerted by the actuator to deform the sample (t denotes the thickness of the prismatic sample along the Z direction). Analytical and experimental results, with the addition of the values provided by technical standard for tests in linear regime.

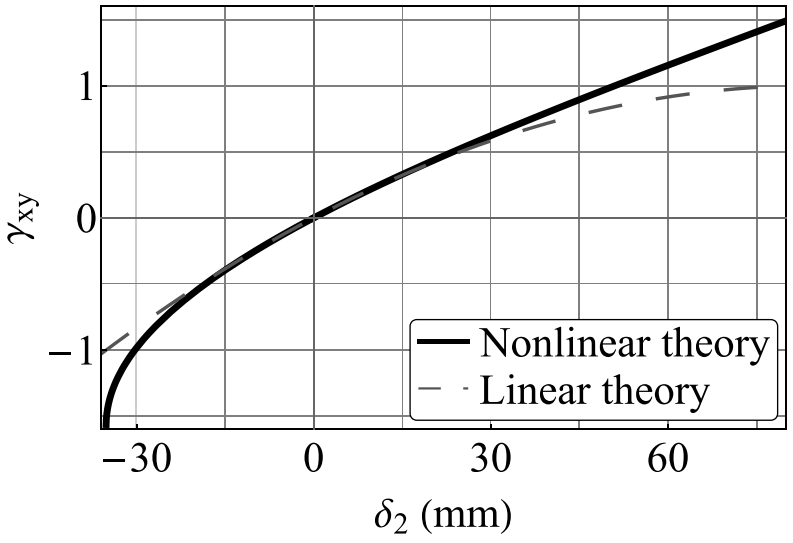

Fig. 13. Comparison between nonlinear and linear γ_{xy}. The latter was used by technical standards to evaluate $\bar{V}$.

compressive loading along a diagonal of a square specimen, causing it to fail in tension (splitting) parallel to the direction of the load (see, for example, RILEM TC. 1994. 76-LUM (1991) and ASTM E 519-02 (2002)). The technical standards provide the following expression for the compressive force: $V' = \sqrt{2}L_t G\gamma'_{xy}$, where G is the shear modulus and $\gamma'_{xy} = (\delta_1 + \delta_2)/L\sqrt{2}$. The normalized force V' is reported in Fig. 12 by a dotted line. Fig. 13 shows the comparison between nonlinear γ_{xy} evaluated by means of (13) and the above linear γ'_{xy}. As the graphs in Figs. 12 and 13 show, when the deformations are small, the values of the force $\bar{V}$ and the angle γ_{xy} coincide.

6. Conclusions

The main difficulty encountered with the simple and pure shear models in finite elasticity lies in the fact that both generate kinematic effects due to angular distortions but also to extension deformations (in a different way). This kinematic coupling can create uncertainties in constitutive modeling and generate difficulties in investigating the shear behavior of a material. These critical issues are overcome by the purely angular shear model, which is based only on the angular variation of linear elements and not on their extension. Specifically, the pure shear of the linearized elasticity has been generalized by only allowing that the shear strains can become large. The biaxial purely angular shear model applied to a cube transforms the base cross section, for example belonging to the XY plane, into a rhombus (whose four sides are equal) by changing only the angle γ_{xy}, now of large magnitude.

By representing the biaxial purely angular shear in the principal reference system, the typical displacement field of some well-known experimental tests, for example the diagonal compression test and the picture frame test, are obtained. Subsequently, the deformation gradient, Green–St.Venant, Piola–Kirchhoff and Cauchy stress tensors were evaluated. In addition, the normal and tangential Cauchy stress vector components on the inclined faces of the deformed cube have been calculated.

In view of the applications and experimental tests, specimens of Dragon Skin FX Pro silicone rubber were created. To constitutively simulate this rubber, the compressible Mooney–Rivlin form has been assigned to the stored energy function.

The cube, subjected to biaxial purely angular shear, has been discretized in order to use the finite element method (FEM). Operationally, a nonlinear incremental analysis is carried out under displacement control. Since the deformation is assumed to be homogeneous, namely independent of the spatial variables, the use of serendipity quadratic shape functions makes the FE solution exact. Therefore, numerical analyses were assigned only the role of checking analytical solutions.

To perform purely angular shear tests a specific testing machine has been designed and built. A rigid steel shearing box, inside which a rubber specimen is positioned, has been realized. An actuator acts on it, imparting the typical deformation of the shear angular model. The test is monitored by a Digital Image Correlation (DIC) system composed of four cameras. The experimental analyses performed reproduced the results of the theoretical analysis with remarkable fidelity.

The results provided by the three different approaches (analytical, numerical, and experimental) were compared with each other. As the imposed vertical displacement varies, the principal stretches (two in-plane components and a third out-of-plane), the principal Cauchy stresses, the volume variation, and the components of the Cauchy stress vector, acting on the inclined faces of the deformed specimen, were compared.

In particular, the analyses showed that, after the initial phase, the normal component of the Cauchy stress vector on the specimen faces, in absolute value, becomes greater than the associated tangential component. These normal stresses are capable of inverting the sign of the horizontal principal stress. This is an interesting aspect to investigate in a nonlinear context, also because there is no equivalent effect for shear tests conducted in linearized elasticity, where these normal stresses are completely absent.

Finally, the external force required to deform the sample was examined. To better highlight the effects of nonlinearities, in this case, the force recommended by current technical standards for linear shear tests was also considered.

In the appendix, some considerations have been formulated for the collapse of the sample at the end of the test.

In conclusion, this paper has provided information for the practical application of the purely angular shear model and has also demonstrated how, from an experimental point of view, this model is much simpler to use than the classical models present in the literature.

CRediT authorship contribution statement

Federico Oyedeji Falope: Investigation, Conceptualization. **Luca Lanzoni:** Methodology, Formal analysis, Data curation. **Angelo Marcello Tarantino:** Validation, Supervision, Project administration.

Declaration of competing interest

The authors declare that they have no known competing financial interests or personal relationships that could have appeared to influence the work reported in this paper.

Acknowledgments

The Italian Ministry of University and Research (MUR) is gratefully acknowledged for the financial support received through the research project FISA-2022-00183 “ Earth-Tech” - Implementation of new Shot-Earth technology in the construction industry, CUP E93C24000250001, and the research grant FIS 2 ”Large and offshore deformations of everyday life: from seismic isolators to person’s health”, project FIS-2023-01661, CUP E53C25000450001.

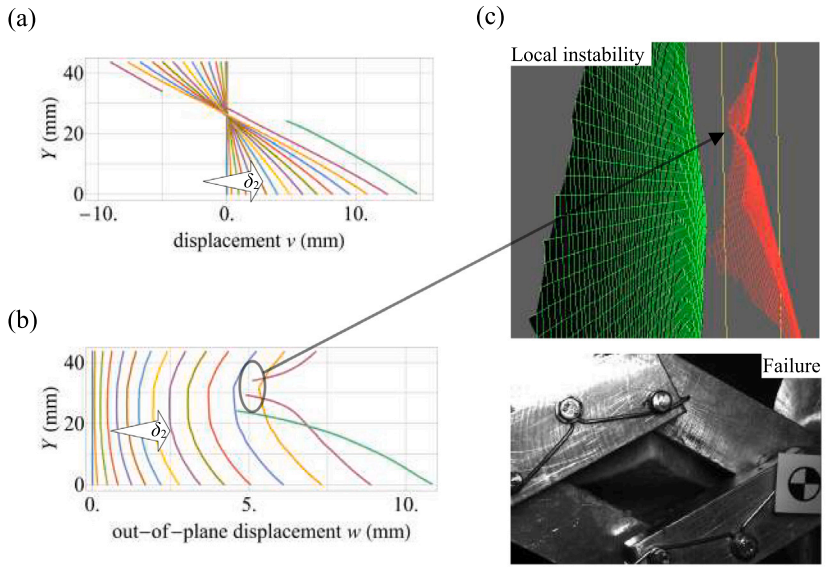

Fig. 14. Failure of the specimen. Vertical displacement profiles associated with the principal stretch λ_2 and out-of-plane displacement w over the vertical virtual gauges reveal the loss of homogeneous character of the deformation as the prescribed displacement varies (a). Detail of the onset of local instability accompanied by the failure of the specimen which comes out of its seat by rotating around the axis of the motion (b). Images of the collapsed specimen (c).

Appendix A. Experimental evidence of the specimen failure

During the experiments, significant issues have been encountered due to the onset of inhomogeneous deformations. The primary cause of such inhomogeneities is the presence of friction on the lateral surfaces of the specimen, in contact with the rigid steel blocks. These undesired frictional effects generate tangential stresses, which overlap with the shear stress (21). The requirement of maintaining this specific shear component, while avoiding the undesired contributions, implies that a lubricated solution cannot be applied to the lateral mantle.

Fig. 14 helps clarify how inhomogeneous deformations arise and develop. The vertical component v of the displacement field is shown in Fig. 14a, along the Y coordinate associated with the vertical gauge in Fig. 6, as the prescribed displacement δ_2 increases. As δ_2 increases, the vertical component v is nearly linear and grows with δ_2, highlighting the compression of the vertical gauge. However, beyond a threshold value of δ_2 a discontinuity in the component v can be observed. This phenomenon becomes clearer by examining the out-of-plane displacement component w, shown in Fig. 14b. For small values of δ_2, the deformation can be considered homogeneous, as indicated by vertical profiles of w. As the deformation increases, friction constrains the specimen ends until a cusp forms. A detailed view of this cusp is provided in Fig. 14c, where both the deformed and undeformed configurations of the specimen are shown, red and green respectively.

Failure of the test occurs as a result of the rotation of the specimen about the principal axis, that initially exhibits a tensile stress (see Fig. 10), causing local instability. It should be noted that this instability is driven by the hydrostatic component of the stress state, which is consistently negative, promoting a reduction in the specimen volume. As a result, the compressed specimen tends to buckle.

Data availability

Data will be made available on request.

References

ASTM E 519-02 (2002). Standard test method for diagonal tension (shear) in masonry assemblages. In *Annual book of ASTM standard*. American Society for Testing and Materials.

Destrade, M., Murphy, J. G., & Saccomandi, G. (2012). Simple shear is not so simple. *Journal of Non-Linear Mechanics*, *47*, 210–214.

Falope, F. O. (2026). The full-field coverage characterization over the energy domain of hyperelastic isotropic materials. *Mechanics of Materials*, *217*, Article 105656.

Falope, F. O., Lanzoni, L., & Tarantino, A. M. (2019). Tarantino, the bending of fully nonlinear beams. Theoretical, numerical and experimental analyses. *International Journal of Engineering Science*, *145*, Article 103167.

Falope, F. O., Lanzoni, L., & Tarantino, A. M. (2024). Energetic exhaustiveness for the direct characterization of energy forms of hyperelastic isotropic materials. *Journal of the Mechanics and Physics of Solids*, *193*, Article 105885.

Falope, F. O., Lanzoni, L., & Tarantino, A. M. (2025). Experiments on the finite torsion of nearly incompressible rubber-like materials: Nonlinear effects, analytic modeling and rubber characterization. *International Journal of Engineering Science*, *211*, Article 104254.

Falope, F. O., Lanzoni, L., & Tarantino, A. M. (2026). Shear models in finite elasticity. *Journal of Elasticity*, 158. http://dx.doi.org/10.1007/s10659-026-10187-3.

Green, A. E., & Zerna, W. (1968). *Theoretical elasticity* (2nd ed.) Oxford: Clarendon.

Gurtin, M. E., Fried, E., & Anand, L. (2010). *The mechanics and thermodynamics of continua*. Cambridge University Press.

Horgan, C. O., & Murphy, J. G. (2010). Simple shearing of incompressible and slightly compressible isotropic nonlinearly elastic materials. *Journal of Elasticity*, *98*, 205–221.

Horgan, C. O., & Murphy, J. G. (2022). Simple shear and applied Piola–Kirchhoff shear stress. *Journal of Elasticity*, *155*, 159–170.

Lanzoni, L., & Tarantino, A. M. (2018). Finite anticlastic bending of hyperelastic solids and beams. *Journal of Elasticity*, *131*, 137–170.

Lanzoni, L., & Tarantino, A. M. (2020a). The bending of beams in finite elasticity. *Journal of Elasticity*, *139*, 91–121.

Lanzoni, L., & Tarantino, A. M. (2020b). Mechanics of high-flexible beams under live loads. *Journal of Elasticity*, *140*, 95–125.

Mihai, L. A., & Goriely, A. (2013). Numerical simulation of shear and Poynting effects by finite element method: An application of the generalised empirical inequalities in non-linear elasticity. *Journal of Non-Linear Mechanics 49*, 1–14.

Moon, H., & Truesdell, C. (1974). Interpretation of adscititious inequalities through the effects pure shear stress produces upon an isotropic elastic solid. *Archive for Rational Mechanics and Analysis*, *55*, 1–17.

Moreira, D. C., & Nunes, L. C. S. (2013). Comparison of simple and pure shear for an incompressible isotropic hyperelastic material under large deformation. *Polymer Testing*, *32*, 240–248.

Ogden, R. W. (1984). *Nonlinear elastic deformations*. Ellis Horwood, Chichester, Reprinted by Dover, New York (1997).

Pelliciari, M., Sirotti, S., & Tarantino, A. M. (2023). A strain energy function for large deformations of compressible elastomers. *Journal of the Mechanics and Physics of Solids*, *176*, Article 105308.

RILEM TC. 1994. 76-LUM (1991). Diagonal tensile strength tests of small wall specimens. In *RILEM: Recommendations for the testing and use of constructions materials* (pp. 488–489). London: E& FN SPON.

Rivlin, R. S. (1948). Large elastic deformation of isotropic materials. IV. Further developments of the general theory. *Philosophical Transactions of the Royal Society 241*, 379–397.

Rivlin, R. S., & Saunders, D. W. (1951). Large elastic deformations of isotropic materials VII. Experiments on the deformation of rubber. *Philosophical Transactions of the Royal Society 243*, 251–288.

Thiel, C., Voss, J., Martin, R. J., & Neff, P. (2019). Shear, pure and simple. *International Journal of Non-Linear Mechanics*, *49*, 57–72.

Treloar, L. R. G. (1944). Stress–strain data for vulcanised rubber under various types of deformation. *Transactions of the Faraday Society*, *40*, 59–70.

Treloar, L. R. G. (1975). *The physics of rubber elasticity*. Oxford: Clarendon.

Truesdell, C., & Noll, W. (1965). *The non-linear field theories of mechanics* (2nd ed.) Berlin: Springer.